Inorganic Chemistry

Forum Article

pubs.acs.org/IC

Restricted Open-Shell Configuration Interaction Cluster Calculations of the L-Edge X-ray Absorption Study of TiO_2 and CaF_2 Solids

Dimitrios Maganas,[†] Serena DeBeer,[†,‡] and Frank Neese*[,†]

[†]Max-Planck Institute for Chemical Energy Conversion, Stiftstrasse 34−36, D−45470 Mülheim an der Ruhr, Germany

[‡]Department of Chemistry and Chemical Biology, Cornell University, Ithaca, New York 14853, United States

Supporting Information

ABSTRACT: X-ray metal L-edge spectroscopy has proven to be a powerful technique for investigating the electronic structure of transition-metal centers in coordination compounds and extended solid systems. We have recently proposed the Restricted Open-Shell Configuration Interaction Singles (ROCIS) method and its density functional theory variant (DFT/ROCIS) as methods of general applicability for interpreting such spectra. In this work, we apply the ROCIS and DFT/ROCIS methods for the investigation of cluster systems in order to interpret the Ca and Ti L-edge spectra of CaF_2 and TiO_2 (rutile and anatase), respectively. Cluster models with up to 23 metallic centers are considered together with the hydrogen saturation and embedding techniques to represent the extended ionic and covalent bulk environments of CaF_2 and TiO_2. The experimentally probed metal coordination environment is discussed in detail. The influence of local as well as nonlocal effects on the intensity mechanism is investigated. In addition, the physical origin of the observed spectral features is qualitatively and quantitatively discussed through decomposition of the dominant relativistic states in terms of leading individual 2p−3d excitations. This contribution serves as an important reference for future applications of ROCIS and DFT/ROCIS methods in the field of metal L-edge spectroscopy in solid-state chemistry.

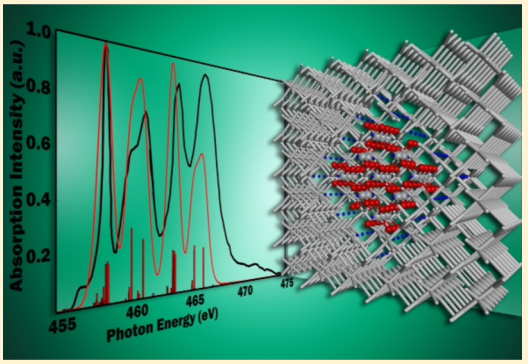

INTRODUCTION

Transition-metal L-edge X-ray absorption spectroscopy is a valuable analytical spectroscopic technique.[1] It is used as a probe of the electronic and geometric structures of materials in an element-specific fashion. Metal L-edge spectra originate from dipole-allowed transitions and feature small intrinsic lines (e.g., the lifetime broadening ranges between 0.2 and 0.6 eV).[2] As such, the metal L-edge spectra are usually richly structured. They are also very sensitive to the metal oxidation and spin state, as well as the local geometric environment surrounding the metallic center. However, the interpretation of the metal L-edge spectra is a challenging task. In addition to ligand-field and covalency effects, one must consider the open-shell $(n-1)p^5nd^{m+1}$ final-state configuration, which may result in many final-state multiplets. Furthermore, the open core-level p shell is subject to strong spin−orbit coupling (SOC), which splits the spectrum into L_3- and L_2-edges and strongly mixes the "nonrelativistic" final states. In that respect, it is only possible to achieve a first-principles quantitative description of the experimental spectra by (a) constructing all possible electron configurations involved in the L-edge excitation process, (b) accounting for the electron dynamic correlation, and (c) properly describing the SOC and covalent interactions. In addition, because metal L-edge spectroscopy is widely applied in the field of solid-state chemistry and heterogeneous catalysis, a successful methodology should also be able to operate on sufficiently large cluster models and in a predictive fashion. A variety of theoretical techniques have been applied to calculate the metal L-edge spectra of several solid systems. In particular, the empirical multiplet approach,[1,3−7] as well as particle/hole-based theories[8−12] and nonempirical configuration interaction (CI) approaches,[13−19] have shown the most successful performance for calculation of the metal L-edge spectra of several open- or closed-shell solid systems. The major drawback of all of these techniques is that they either are not able to treat the metal L-edge problem of molecules and solids in a universal manner or are computationally too demanding for large-scale applications.

For example, in the field of solid-state chemistry, the atomic multiple theory has been successfully applied to treat the Ca L-edge spectra of CaF_2 and CaO,[19,20] while it has shown a much worse performance for calculation of the Ti L-edge spectra of $SrTiO_3$ and anatase TiO_2.[19] Nevertheless, because this method is heavily parametrized, it is valuable for interpretation purposes but has limited predictive capabilities, in particular for low-symmetry systems. A common practice to overcome this deficiency is to compare the atomic multiple theory results with

Special Issue: Insights into Spectroscopy and Reactivity from Electronic Structure Theory

Received: January 25, 2014
Published: May 28, 2014

   dx.doi.org/10.1021/ic500197v | Inorg. Chem. 2014, 53, 6374−6385

those obtained by ab initio CI techniques[15,19,20] such as those developed by Ogasawara et al.[13,17,19]

The latter methodology relies heavily on the framework of a molecular *jj* coupling scheme in which SOC is introduced at the level of one-particle orbitals. This technique has shown satisfactory performance for many solid systems including CaF_2 and TiO_2;[15,19,20] however, it can only be applied to very small cluster models containing, at most, one to three metal centers. Hence, this approach does not allow solid-state effects to be properly treated. In addition, in order to make the calculation feasible, the CI space is usually truncated to essentially only include the d−d excitation space. Therefore, a large proportion of the dynamic correlation is not considered, which is of questionable accuracy, in particular for more covalent systems. Alternative CI techniques based on molecular *jj* coupling[21] or plane-wave density functional theory (DFT) using projection methods to obtain a localized expansion space[22] have also been proposed, but they appear to be restricted to highly symmetric molecules and require significant computational resources.

On the other hand, in order to deal with the size of the treated cluster, techniques of the particle/hole type have been employed based on time-dependent DFT,[8,9] the multichannel multiple scattering[23−25] and the Bethe−Salpeter equations.[26,27] These techniques have also shown satisfactory performance in treating the metal L-edge spectra of many transition-metal solids.[8,15,20,23] However, it should be emphasized that the space of singly excited determinants only spans a small part of the final-state manifold that is reached in L-edge absorption spectroscopy and thus, in general, these techniques will necessarily miss many spectral features that are observed in the experimental data. This problem is not acute for closed-shell systems but is of dominant importance for open-shell species.

Thus, despite the existence of several important and useful theoretical methods, the lack of a globally satisfactory methodology to treat the metal L-edge problem of solids remains a challenge. The problem could be adequately addressed in the framework of a multideterminatal ab initio theory, as long as this is applicable to large polymetallic systems. With all of these factors in mind, we have recently introduced the DFT/Restricted Configuration Interaction Singles (ROCIS) method as an alternative approach to the transition-metal L-edge problem. DFT/ROCIS is a method that is conceptually based on correlated wave function methodology. The method relies heavily on the Molecular LS (Russell−Saunders) coupling scheme in which SOC is introduced at the level of many-particle configuration state functions (CSFs). In addition, it has been shown to have a strong predictive performance and can be applied to cluster systems with about 100−200 atoms.[28,29] It should be emphasized that, because the ROCIS and DFT/ROCIS methods are based on a high-spin-coupled restricted open-shell determinant, it will apply to many systems but naturally not to all systems. Complicated systems, such as antiferromagnetically aligned solids, will likely remain inaccessible by either method in the foreseeable future. The implementation and application of this methodology to a variety of coordination complexes and cluster systems has recently been explored.[28,30,31] Inspired by the excellent performance of DFT/ROCIS methodology for the recently reported calculations of the metal L-edge NEXAFS spectrum of V_2O_5,[28] in this work we describe an analogous study of the metal L-edge spectra of CaF_2, as well as the rutile and anatase polymorphs of TiO_2.

COMPUTATIONAL METHODOLOGY

All calculations were performed by the *ORCA* suite of programs.[32] DFT/ROCIS calculations were performed by employing the converged restricted Kohn−Sham RKS wave functions using the B3LYP[33−35]/def2-TZVP[36,37] basis sets of triple-ζ quality[38] together with the auxiliary basis set def2-TZVP/J in order to accelerate calculations in the framework of RI approximation. For embedded cluster calculations, capped effective core potentials (c-ECPs) were used to replace the metal (ECP10MDF)[39] and oxygen (ECP2MWB)[40] atoms, respectively. The cluster models for this study are described in detail below. The calcium, fluorine, titanium, and oxygen atomic positions were taken from the experimental X-ray bulk structures of CaF_2,[41] TiO_2 rutile,[42] and TiO_2 anatase.[42] In order to calculate the absorption intensities, the orbitals from the converged restricted open-shell Hartree−Fock (ROHF) or DFT self-consistent-field (SCF) orbitals were localized according to the Pipek−Mezey localization scheme.[43] Each calculated spectrum involves excitations from either a single or up to six metal atoms, and the total spectra correspond to a sum over the individually calculated spectra. In order to ensure saturation of the final-state manifold, the relativistic states are calculated on the basis of 40−80 nonrelativistic roots per multiplicity. Unless otherwise stated in the text, all of the spectra are shifted to match the experimental counterpart at the peak position of the L_3 region. Such a shift is necessary because the calculated absolute transition energies carry errors that arise from shortcomings of the density functionals in the core region, limitations of the one-particle basis set, and shortcomings in the accurate modeling of spin-free relativistic effects. These errors are usually highly systematic, and, in fact, all of these factors can (for a given basis set and density functional) be taken into account by introducing an element-dependent shift.[44−48] Although ways to avoid the introduction of such an empirical shift have been proposed,[49] it has been shown that a simple linear regression is sufficient to establish predictive accuracy in the calculated transition energies for any given element.[30,44,48,50] This calibration needs to be carried out with respect to a test set of well-known systems and has already been reported for metal and ligand K-edges in the framework of scalar relativistic DFT methodology,[44−46,48] as well as for V L-edge spectra in the framework of DFT/ROCIS methodology.[30] In this work, we take the liberty to treat such a shift as an empirical parameter, and the corresponding value for each of the employed clusters is provided in Table 1. The SOC-corrected absorption spectra were obtained from ROCIS- or DFT/ROCIS-calculated intensities by applying a Gaussian broadening to the calculated transitions in the range 0.2−0.4 eV in order to visually match the main signals, as close as possible.

Table 1. Shifts Applied to Experimental and Calculated Transitions for V L-Edge and O K-Edge Absorption Spectra

cluster model	M $L_{2,3}$-edge shift
$Ti_{13}O_{52}H_{78}$	12.21
$Ti_{15}O_{30}H_{28}$	12.50
$[(Ca_8F_{40})^{-24} + (BR_1 + PC_1)]^0$	−6.21
$[(Ca_9F_{48})^{-30} + (BR_2 + PC_2)]^0$	14.49
$[(Ti_{23}O_{80})^{-68} + (BR_3 + PC_3)]^0$	12.31
$[(Ti_{15}O_{56})^{-52} + (BR_4 + PC_4)]^0$	12.52

PC_1 = 747, PC_2 = 921, PC_3 = 1523, and PC_4 = 4501. BR_1 = 75, BR_2 = 43, BR_3 = 95, and BR_4 = 79.

GEOMETRIC PROPERTIES

CaF_2 is an ionic lattice with a face-centered-cubic structure. The unit cell of the material is most easily described as a simple cubic lattice formed by the fluorine atoms, where a calcium atom is contained in every second cube. The lattice constant is a = 5.451 Å, as can be seen in Figure 1. Along the 111 direction, the lattice is built in such a way that each calcium atom is

dx.doi.org/10.1021/ic500197v | Inorg. Chem. 2014, 53, 6374−6385

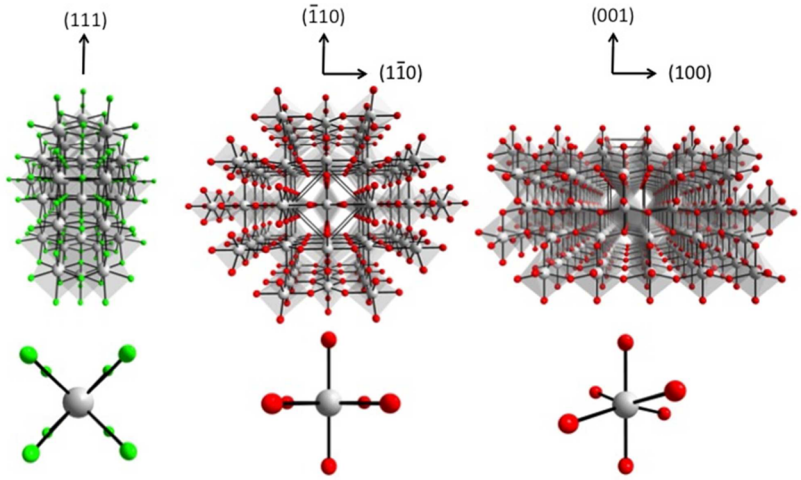

Figure 1. Crystallographic structures of CaF_2 (left), TiO_2 rutile (middle), and TiO_2 anatase (right), which grow as extended networks along the (111), (1$\bar{1}$0)($\bar{1}$10), and (100) and (001) directions, respectively. The corresponding repeated cubic CaF_8 and octahedral TiO_6 cores are also illustrated.

coordinated to eight fluorine atoms, while each fluorine atom is tetrahedraly coordinated to four calcium atoms (Ca−F = 1.964 Å).[41] On the other hand, the TiO_2 crystal exhibits three polymorphs, namely, rutile, anatase, and brookite. Among them, rutile is the thermodynamically stable one, while anatase and brookite are metastable polymorphs. Rutile and anatase are both crystallized in tetragonal space groups $P4_2/mmm-D_{4h}^{14}$ and $I4_1/amd-D_{4h}^{19}$, respectively,[42] forming TiO_6 octahedral units, and they are widely used in industrial applications.[51] In rutile, the TiO_6 building units are axially elongated with different axial and equatorial Ti−O bond lengths (Figure 1b; Ti−O_{ax} = 1.984 Å and Ti−O_{eq}= 1.944 Å). As a result, the symmetry is lowered from O_h to D_{2h}. In anatase, additional displacements of the oxygen atoms from the equatorial positions further lower the local symmetry around titanium to C_{2v} (Figure 1c; Ti−O_{ax} = 1.964 Å, Ti−O_{eq}= 1.937 Å, and O_{eq}−Ti−O_{eq} = 155°).

CONSTRUCTION OF CLUSTER MODELS

The cluster models that mimic the local environments of the CaF_2 (111) crystal direction were constructed using the effective core potential embedding approach. In the most popular variant of this approach,[28,52] the quantum cluster (QC) is embedded in an extended point charge (PC) field. Furthermore, in order to avoid electron attraction or electron flow from the QC region toward the positive charges at the PC region, a third boundary region (BR) is introduced between the QC and PC and is constructed from repulsive capped effective core potentials (c-ECPs). The employed embedded scenario is graphically presented in Scheme1. As is seen in Figure 2a, the QC $[Ca_8F_{40}]^{24-}$ was chosen to represent the (111) direction of CaF_2. This was embedded in a PC field consisting of 747 PCs (q_{Ca} = 1.41; q_F = −0.99). The coordinates of the charges to construct the PC field are taken from the crystallographic coordinates of the corresponding atoms. These charges are then optimized using the criterion of neutrality according to the relation $q_{QC} = -(q_{BR} + q_{PC})$, where q values are the respective total charges (Scheme1). As in our previous V_2O_5 study,[30] several variants of charge combinations were tested and the calculated spectra were compared. In general, charge combinations that are close to the electrostatic charges that arise within a SCF calculation are the preferable choices and provde the most balanced description of the embedded

Scheme 1. Schematic Representation of the General Embedded Method Employed, as Well as the Applied Charge Neutralization Scenario

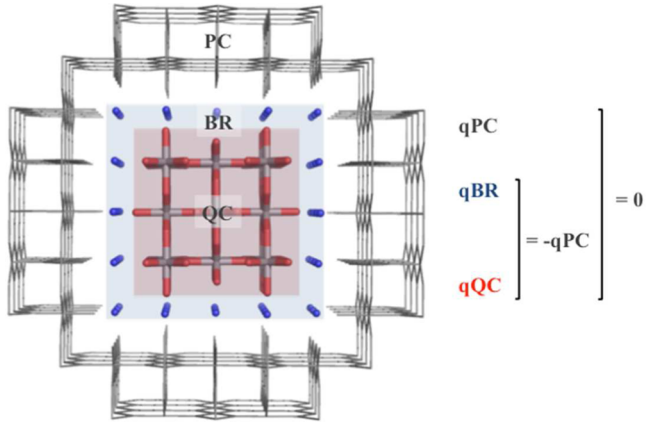

cluster.[30,31] In addition, as will be discussed in more detail in the Results section, for comparison reasons between the performance of the ROCIS and DFT/ROCIS methods in ionic cases, the QC $[Ca_9F_{48}]^{30-}$ was also constructed and embedded in a PC field (with optimized charges q_{Ca}=1.40 and q_F = −0.98) constructed by 921 PCs (Figure 2b). The cluster models to mimic the local environments of rutile and anatase TiO_2 were constructed by using both the hydrogen saturation and effective core potential embedding techniques.[28,52] The hydrogen saturation technique has been proven to be a valid method to describe metal L-edge X-ray spectroscopic properties of strongly covalent metal oxide systems such as V_2O_5 and TiO_2.[8,28,31,53,54] This technique implies that hydrogen atoms saturate the dangling bonds of the constructed clusters. In this work, the $Ti_{13}O_{52}H_{78}$ and $Ti_{15}O_{30}H_{28}$ clusters (shown in Figure 3a,c) were chosen to represent the TiO_2 rutile and anatase polymorphs, respectively. In an analogous way, the cluster models $[Ti_{23}O_{80}]^{68-}$ and $[Ti_{15}O_{56}]^{52-}$ were also considered and embedded in PC fields constructed by 1523 (q_{Ti} = 2.18; q_O = −1.24) and 4501 (q_{Ti} = 2.54; q_O = −1.46) PCs, respectively (Figure 3c,d).

dx.doi.org/10.1021/ic500197v | Inorg. Chem. 2014, 53, 6374−6385

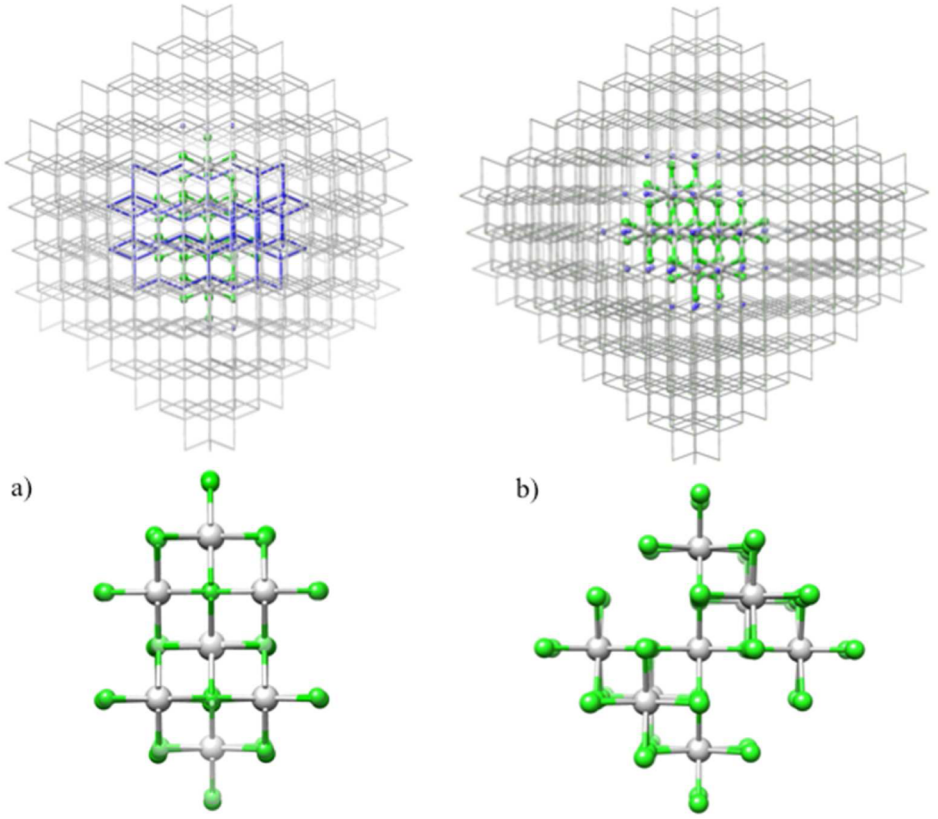

Figure 2. Geometries of embedded cluster models representing the CaF_2 (111) direction. (a) $[Ca_8F_{40}]^{24-}$ cluster embedded in a PC field with BR_1 = 78 and PC_1 = 748 (q_{Ca} = 1.40; q_F = −0.98). (b) $[Ca_9F_{48}]^{30-}$ cluster embedded in a PC field with BR_2 = 42 and PC_2 = 921 (q_{Ca} = 1.41; q_F = −0.99).

■ ELECTRONIC STRUCTURE

Ca^{II} and Ti^{IV} in cubic (CaF_8) and distorted octahedral (TiO_6) networks have ground states with $2p^63d^0$ electron configurations. Upon 2p electron excitation, the resulting final states belong to the $2p^53d^1$ electron configuration. The qualitative nature of the involved 2p3d one-electron excitations can, to a first approximation, be explored within a ligand-field theory (LFT) type of analysis. As has been discussed already for many systems,[1,28,30] the atomic multiplets that arise from the $2p^53d^1$ electron configuration are $^2P \otimes {}^2D = {}^{1,3}P, {}^{1,3}D, {}^{1,3}F$. These atomic states can be transformed into molecular ones upon consideration of the symmetry of the CaF_8 and TiO_6 cores. Within the one-particle approximation for CaF_2 and TiO_2 rutile and anatase, these states are presented in Figure 4. It has been shown[19] that the 8-fold cubic symmetric CaF_8 unit has a cubic (or reversed O_h) crystal-field splitting. Under O_h symmetry, the spatial components of the angular momentum transform as T_{1u}. As a result, the final states of the $2p^53d^1$ electron configuration are grouped as $^{1,3}A_{1u} + {}^{1,3}E_u + {}^{1,3}T_{1u} + {}^{1,3}T_{2u}$ ($2p_{x,y,z} \rightarrow 3d_{xy,xz,yz}$) and $^{1,3}T_{1u} + {}^{1,3}T_{2u}$ ($2p_{x,y,z} \rightarrow 3d_{x^2-y^2,z^2}$). Likewise, in the D_{2h} and/or C_{2v} point groups, the three components of the angular momentum operator transform as $\mathbf{L}_x$, B_{3g}; $\mathbf{L}_y$, B_{2g}; $\mathbf{L}_z$, B_{1g} and as $\mathbf{L}_x$, B_2; $\mathbf{L}_y$, B_1; $\mathbf{L}_z$, A_1. Both the T_{1g} and T_{2g} states (in O_h symmetry) map onto $^{1,3}T^z_{1,2}$:$^{1,3}B_{1g}$/$^{1,3}A_1$,$T^y_{1,2}$:$^{1,3}B_{2g}$/$^{1,3}B_1$,$T^x_{1,2}$:$^{1,3}B_{3g}$/$^{1,3}B_2$ states under D_{2h} and C_{2v} symmetry, respectively. The important single-electron excitations are those arising from the doubly occupied to the virtual/empty molecular orbitals (MOs) of type doubly occupied molecular orbital−virtual molecular orbital, and they are presented in Figure 4. In both cases, the action of SOC will further split these molecular states into molecular magnetic sublevels $|0\rangle$, $|\pm1\rangle$ characterized by quantum numbers M_S = 0, ±1. It should be highlighted, however, that, within such an oversimplified excitation scheme, the L_3/L_2 ratio of the NEXAFS spectrum of all of the transition elements would be 2/1. Nevertheless, the one-electron picture is still useful for a qualitative description of the experimental and calculated spectra. At this level and under approximate O_h and D_{2h} and/or C_{2v} symmetries, as shown in Figure 4, the TiO_2 Ti L-edge spectra are expected to be more complicated with respect to the corresponding Ca L-edge spectrum containing at least five excitations per polarization and spin multiplicity: $^1A_1 \rightarrow 3^{1,3}(B_2 + A_1 + A_2 + B_1)$ corresponding to the $2p_{x,y,z} \rightarrow 3d_{xy,xz,yz}$, $d_{x^2-y^2}$, and d_{z^2} single-electron excitations, respectively. Within the applied LS coupling scheme defined by DFT/ROCIS, five classes of single and double excitations are considered in order to construct the initial CSFs. In addition, the complete number of unoccupied orbitals enters the active CI space in order to properly account for electron correlation and covalency.[29,31] Initially, the nonrelativistic states of the same and higher (and/or lower) spin multiplicities with respect to the ground state are evaluated on the basis of the above CI electron excitation pattern involving spin-conserving and spin-flip excitations. The final SOC relativistic states are generated by the quasi-degenerate perturbation theory (QDPT), in combination with a mean-field approximation to the full two-body SOC operator.[55−57]

■ RESULTS

XAS Spectra. The experimental spectra of bulk CaF_2 and TiO_2 rutile and anatase are shown in Figure 5. The spectrum of CaF_2 was obtained from previous studies of Shirley[26] and Himpsel et al.,[26,58] whereas the Ti L-edge spectra of TiO_2 rutile

dx.doi.org/10.1021/ic500197v | Inorg. Chem. 2014, 53, 6374−6385

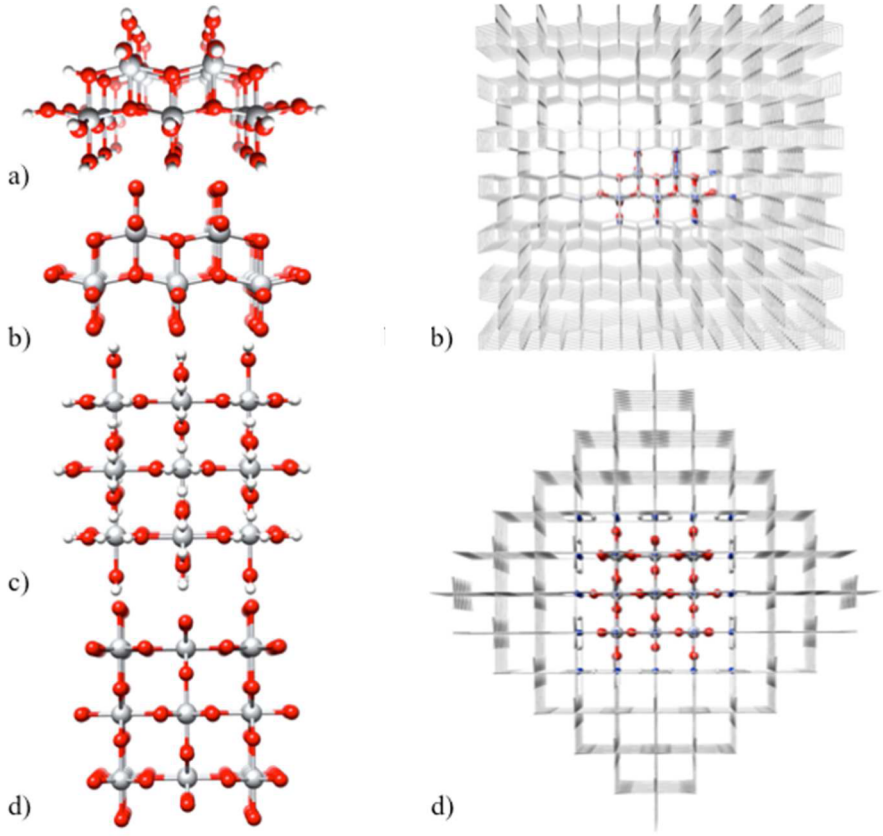

Figure 3. Geometries of embedded cluster models representing the TiO_2 (100) direction for rutile and anatase. (a) $[Ti_{23}O_{80}]^{68-}$ cluster embedded in a PC field with BR_3 = 78 and PC_3= 1523 (q_{Ti} = 2.18; q_O = −1.24). (b) The $[Ti_{15}O_{56}]^{52-}$ cluster embedded in a PC field and (d) with BR_4 = 42 and PC_4 = 4501 (q_{Ti} = 2.54; q_O = −1.46). Geometries of the hydrogen-saturated cluster models for TiO_2 rutile (c, $Ti_{13}O_{52}H_{78}$) and TiO_2 anatase (d, $Ti_{15}O_{30}H_{28}$).

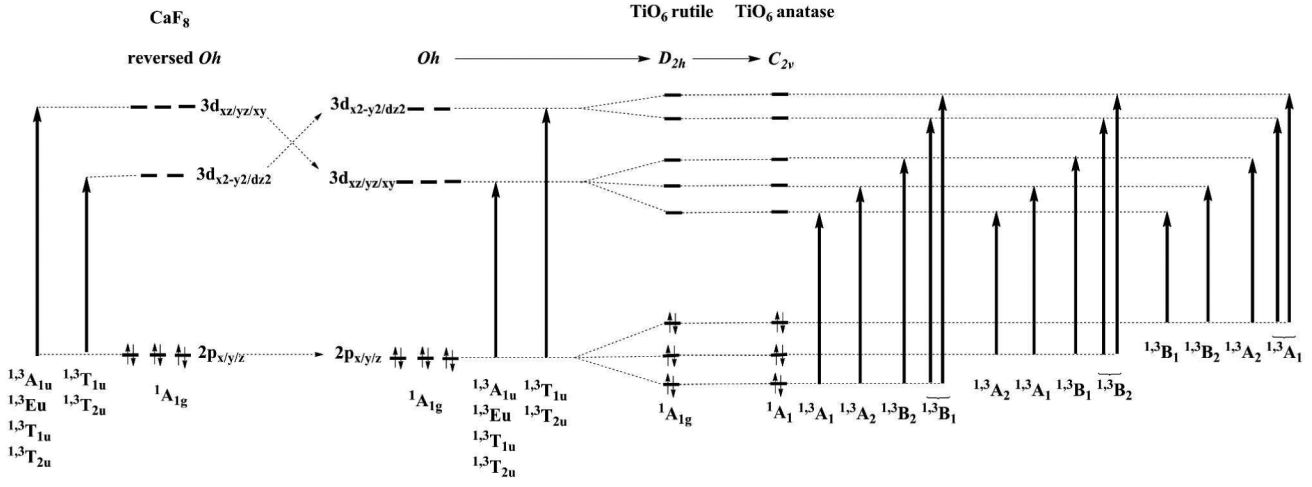

Figure 4. MO splitting diagram of the local CaF_8 (O_h) and TiO_6 rutile (D_{2h}) and anatase (C_{2v}) cores. In addition, the adapted 2p−3d transitions in the one-electron particle/hole approximation are visualized assuming ideal reversed O_h, O_h, D_{2h}, and C_{2v} ligand-field splittings.

and anatase were obtained from reports by van der Laan.[59] We should emphasize that the Ti L-edge spectra from the latter study are very similar to the recently reported spectra for TiO_2 rutile (110) and TiO_2 rutile (001).[60] Such relevance between the spectra and crystal directions will be thoroughly investigated below. It is well-known that the metal L-edge spectra usually consist of two main signal regions belonging to the low-energy L_3 and high-energy L_2 spectral regions. Among these regions, L_3 is in most of the cases highly resolved and, thus, provides information regarding the ligand-field splitting of the coordination environment around the metal center. On the other hand, in the L_2 region, the corresponding information is usually obscured because of the presence of the Coster−Kronig Auger decay channels.[61] As is seen in Figure 5, the bulk CaF_2 spectrum contains a total of seven distinguishable signals. Four of them lie in the L_3 region at 346.6, 347.4, 348.2, and 349.1 eV and another three in the L_2 region at 351.0, 351.6, and at 352.5 eV. According to Himpsel's experimental analysis,[58] the signals

dx.doi.org/10.1021/ic500197v | Inorg. Chem. 2014, 53, 6374−6385

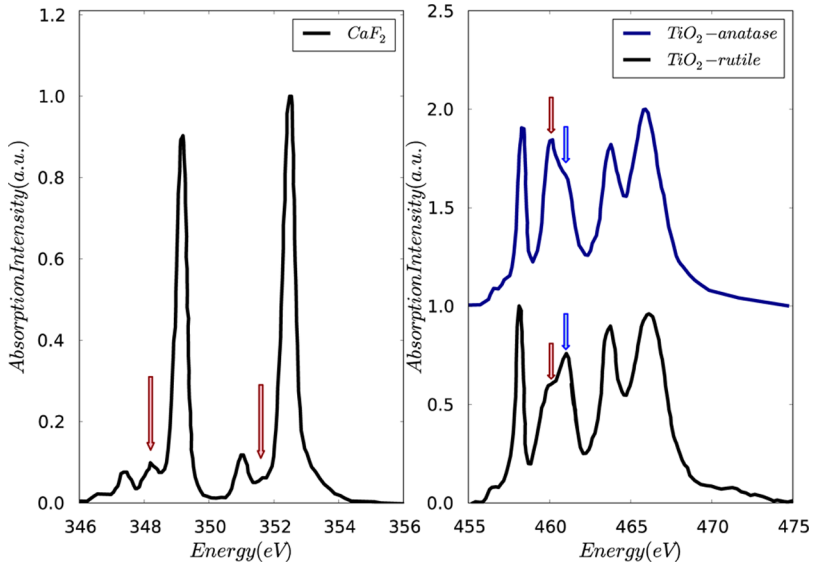

Figure 5. Experimental Ca and Ti L-edge spectra for bulk CaF_2[58] and TiO_2 anatase[59] and rutile,[59] respectively. Red and blue arrows indicate signal enhancements and dienhancements due to bulk/surface and/or local and nonlocal interactions.

located at 348.2 and 351.6 eV, marked with red arrows in Figure 5 (left panel), correspond to enhancements due to surface or bulk interactions within the crystal lattice. In addition, the experimental spectra of TiO_2 rutile and anatase are presented with black and dark-blue lines, respectively, in Figure 5 (right panel) and are also characterized by seven distinguishable signals. In particular, the L_3 region contains two satellite signals at 456−457 eV, one sharp, high-intensity signal at 458 eV, and two overlapping signals at 460 and 461 eV. The L_2 region, on the other hand, is less informative because of extra broadening. Therefore, only two well-separated signals are observed at 463.5 and 465 eV. The most pronounced difference between rutile and anatase is reflected in the overlapping signals of the L_3 region located at 460 and 461 eV (as indicated in Figure 5 with red and blue arrows, respectively). It is well-known that for rutile and anatase the intensities of these signals are interchanged. The origin of such a difference has been assigned to nonlocal, long-range interactions with the neighboring titanium atoms.[23,62,63] In an alternative scenario, this difference is attributed to local ligand effects arising, for example, from different O_h distortions around titania centers for rutile and anatase.[64,65] Such distortions, however, have been questioned as being too small to explain the splitting of the signal around 460−461 eV.[62] Recently, the first assumption has gained ground over the second one, after the important contribution by Krüger.[23] His study, based on multichannel multiple-scattering calculations,[24,25] confirmed that indeed nonlocal effects are present. In addition, it was shown that for rutile these effects scale up to about 1 nm length (cluster size of about 60 atoms) before they converge and provide the correct shape of this signal. Evidently, local and nonlocal interactions seem to play an important role in explaining the metal L-edge spectroscopy for solids. In an attempt to clarify this point further, the above-mentioned quantities are investigated below for both CaF_2 and TiO_2 L-edge spectra in the framework of the ROCIS and DFT/ROCIS methodologies.

Effect of the Coordination Environment. *CaF_2.* For calculation of the Ca L-edge spectrum, we first employ the $[(Ca_8F_{40})^{24-} + (BR_1 + PC_1)]$ embedded cluster within the ROCIS approach. By using ROHF orbitals and a cluster embedded in an ionic PC field, the most ionic description of the calculated Ca L-edge spectrum can be accomplished. We have furthermore used a tight BR_1 region (consisting of 75 atoms) to prevent charge flow from the PC region to the QC region and vice versa. As can be seen in Figure S1 (Supporting Information), satisfactory agreement between the calculated Ca L-edge spectrum and the experimental one is observed. As expected, the SOC is underestimated by about 3−4%;[28,31] thus, the calculated L_2 spectrum, after the L_3 highest-intensity feature is matched with the corresponding experimental one, is slightly shifted to lower energies. More specifically, all of the visible experimental features are reproduced, while the calculated relative intensities of the main signals agree well with the experimental ones. As can be seen in Figure S1 (Supporting Information), each calcium center within the $[(Ca_8F_{40})^{24-} + (BR_1 + PC_1)]$ cluster model contributes equally to the total intensity of the spectrum, indicating that the observed Ca L-edge spectrum corresponds essentially to an isolated $[CaF_8]$ center and is not sensitive to the coordination environment beyond the first coordination sphere. However, the ROCIS method predicts the wrong relative intensities for certain spectral features, indicating that this approach is still too ionic to correctly describe the entire spectrum. In particular, the signals at 348.2 and 351.6 eV are either predicted with unrealistic low intensity and/or shifted to higher energies and obscured under the intensity of the main L_2 feature. This is not surprising within the applied HF-based methodology. Moreover, this suggests that at least a certain amount of Ca−F bond covalency exists and should be properly treated (e.g., within the DFT/ROCIS methodology).

In order to treat such covalent interactions, the $[(Ca_9F_{48})^{30-} + (BR_2 + PC_2)]$ embedded cluster is employed (Figure 2b). This cluster contains a central $[CaF]_8$ center surrounded by another eight units of the same composition. This embedded cluster is constructed with a smaller boundary region (BR_2 = 43 atoms) compared to $[(Ca_8F_{40})^{-24} + (BR_1 + PC_1)]$ and is embedded in an ionic PC field (q_{Ca} = 1.41; q_F = −0.93). Because of some charge flow between the PC and QC regions, the calcium centers experience a stronger ionic environment in the B3LYP SCF calculation. In particular, the central calcium

dx.doi.org/10.1021/ic500197v | Inorg. Chem. 2014, 53, 6374−6385

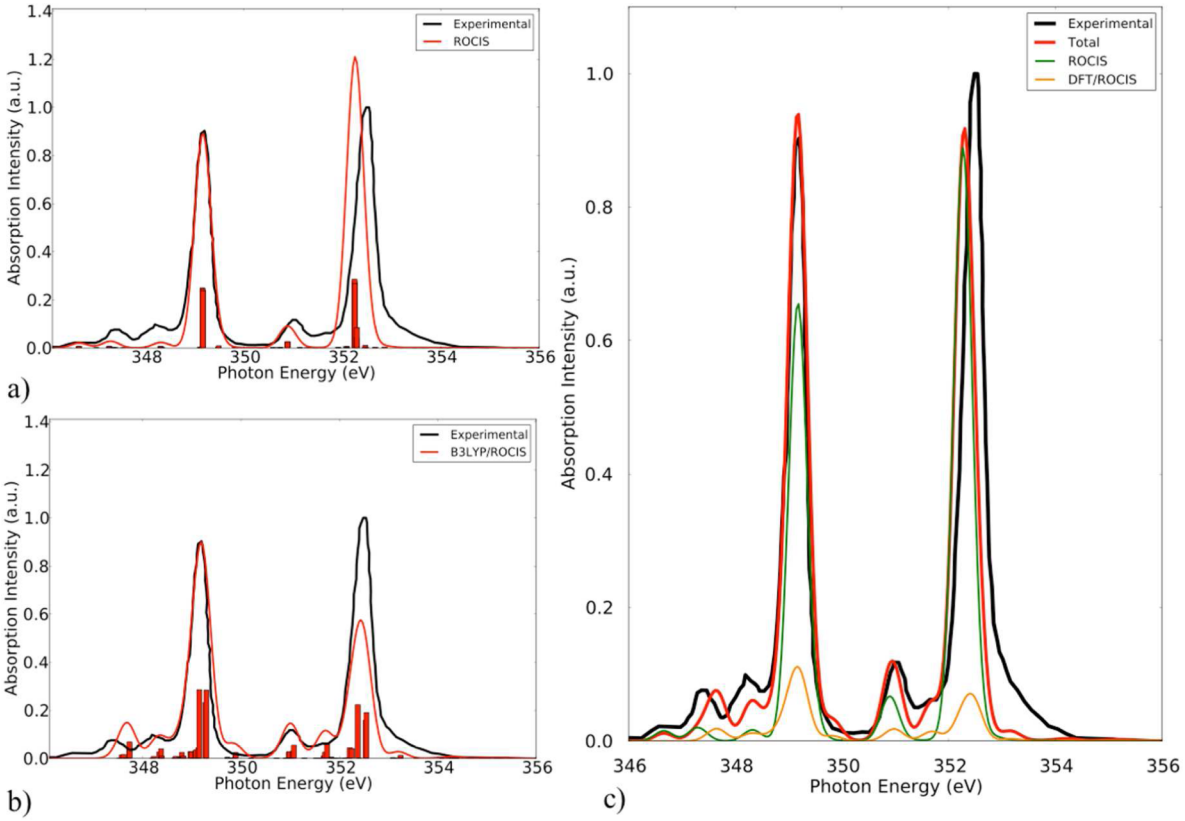

Figure 6. Experimental (black line) versus calculated (red line) (a) ROCIS [def2-TZVP(-f)] and (b) DFT/ROCIS [B3LYP/def2-TZVP(-f)] Ca L-edge spectra of the $[(Ca_9F_{48})^{30-} + (BR + PC_2)]$ model. The calculated spectra correspond to the central calcium center. (c) Red line corresponding to the summation of spectra shown in parts a (green) and b (orange), assuming an 8:1 contribution in the $[(Ca_9F_{48})^{30-} + (BR + PC_2)]$ cluster model.

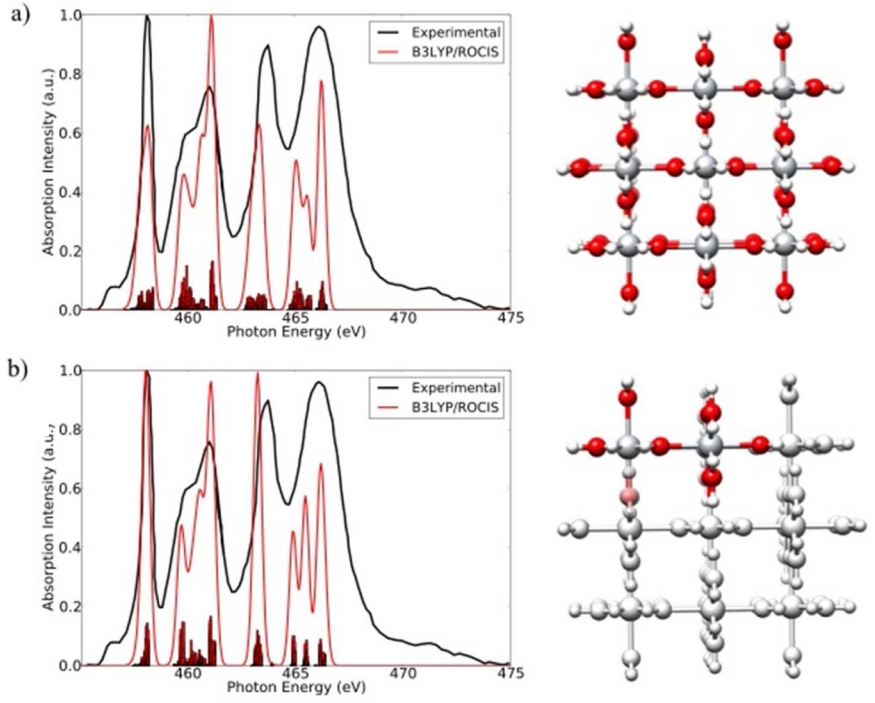

Figure 7. Experimental (black line) versus calculated (red line) B3LYP/ROCIS [def2-TZVP(-f)] Ti L-edge spectra of the $Ti_{13}O_{52}H_{78}$ cluster model: (a) calculated spectrum containing contributions from the 13 titanium centers; (b) calculated spectrum corresponding to repeated $[Ti_2O_{10}H_{14}]$ units.

dx.doi.org/10.1021/ic500197v | *Inorg. Chem.* 2014, 53, 6374−6385

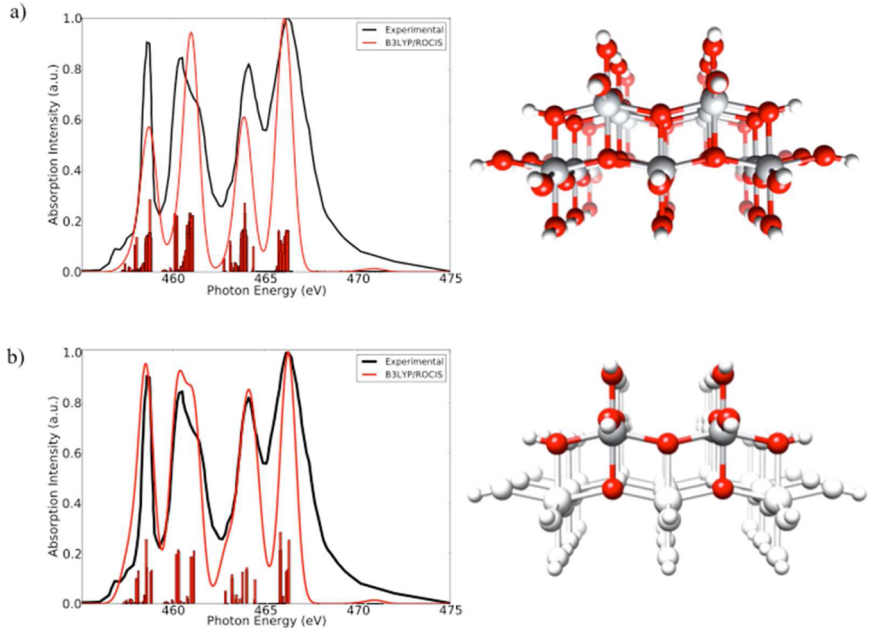

Figure 8. Experimental (black line) versus calculated (red line) B3LYP/ROCIS [def2-TZVP(-f)] Ti L-edge spectra of the $Ti_{15}O_{30}H_{28}$ cluster model: (a) calculated spectrum containing contributions from the 15 titanium centers; (b) calculated spectrum corresponding to repeated $[Ti_2O_{10}H_8]$ units.

center reaches ionic charge values very close to those obtained by the ROHF method ($q_{Ca,Mulliken}$ = 0.8). The calculated ROCIS spectrum is identical with the corresponding spectra arising from the CaF_8 fragments of the $[(Ca_8F_{40})^{-24}$ + (BR_1 + PC_1)] model (Figure S1 in the Supporting Information). On the other hand, the B3LYP/ROCIS Ca L-edge spectrum dominated by this particular central calcium center contains intensity-enhanced features (Figure 6b) compared with the corresponding ROCIS spectrum (Figure 6a). This leads, in general, to better agreement with respect to experiment for those features. We should further note that such a behavior is not unexpected because, in general, DFT/CI techniques, operating on fully ionic embedded models (e.g., the cluster model is embedded directly in a PC field constructed from formal charges), have been proven successful to calculate the Ca L-edge spectrum of CaF_2.[14,19] In particular, the signals at 346.6 and 347.4 eV merge together to a signal at 347.6 eV, while the mirror signal at 351 eV is predicted with the correct intensity. Furthermore, it should be noted that the intensity of the main L_2 signal located at 352.5 eV is strongly underestimated. It should be emphasized, however, that the energy position and/or the intensities of the L_2 region are subject to distortions and broadening because of the Coster−Kronig Auger decay,[61] which cannot be estimated accurately by experiment and is not treated at all within the DFT/ROCIS framework.[31] Most importantly, the signals at 348.2 and 351.6 eV, which originate from surface interactions,[20,58] are now clearly present, indicating that these signals are affected not only from the local coordination environment around the calcium centers (e.g., surface effects due to lower symmetry)[20] but also from the strength of the Ca−F interactions. In a sense, it seems that the ROCIS method provides information about the spectral features corresponding to isolated CaF_8 units, while the DFT/ROCIS method provides spectral information related to interfragment communication through a second coordination sphere, bulk effects, and so on. For example, relevant effects have been shown to be important in order to correctly describe the V L-edge spectrum in V_2O_5.[28] Furthermore, although in the case of CaF_2 these effects are approached with two different methods (ROCIS and DFT/ROCIS), they can be qualitatively combined by considering the calcium composition in the $[(Ca_9F_{48})^{30-}$ + (BR_2 + PC_2)] embedded cluster. Thus, in Figure 6c, the spectra of Figure 6a,b are plotted with an intensity ratio of 8:1. The resulting combined calculated spectrum provides satisfactory agreement with respect to the experimental one, indicating that the experimental spectrum is primarily dominated by isolated CaF_8 units, containing significant contributions from bulk covalent Ca−F interactions.

TiO_2. a). Hydrogen-Saturated Clusters. The Ti L-edge spectrum of TiO_2 rutile is first calculated by employing the hydrogen-saturated $Ti_{13}O_{52}H_{78}$ cluster and is visualized in Figure 7a. It can be clearly seen that the main spectral features are successfully reproduced including the satellite signals located at 456−457 eV. These later signals are, however, shifted at higher energies and overlapping with the signal at 458 eV. In addition, the splitting and relative intensities of the overlapping signals at 460−461 eV are successfully interpreted. We notice, however, that the relative intensities of the signals at 458 and 461 eV are not correct. Furthermore, in order to arrive at spectral convergence with respect to the size of the cluster, individual atom contributions were considered. That was performed by monitoring local excitations from specific centers, from calculations performed over the full excitation space of the metal clusters. Analysis of the individual atom contributions reveals that the best agreement between calculated and experimental spectra in terms of relative intensities is accomplished by considering repeated dimeric species $[Ti_2O_{10}H_{14}]$, as is seen in Figure 7b. In an analogous way, the Ti L-edge spectrum of TiO_2 anatase was calculated by employing the $Ti_{15}O_{30}H_{28}$ cluster visualized in Figure 8a. As in the case of TiO_2 rutile, the main experimental features are successfully predicted. However, certain relative intensities corresponding to the splitting of the overlapping signals at 460 and 461 eV, as well as the intensities of the signals located at 458 and 461 eV, are incorrect. Once again, better agreement between theory and experiment is observed when dimeric

dx.doi.org/10.1021/ic500197v | Inorg. Chem. 2014, 53, 6374−6385

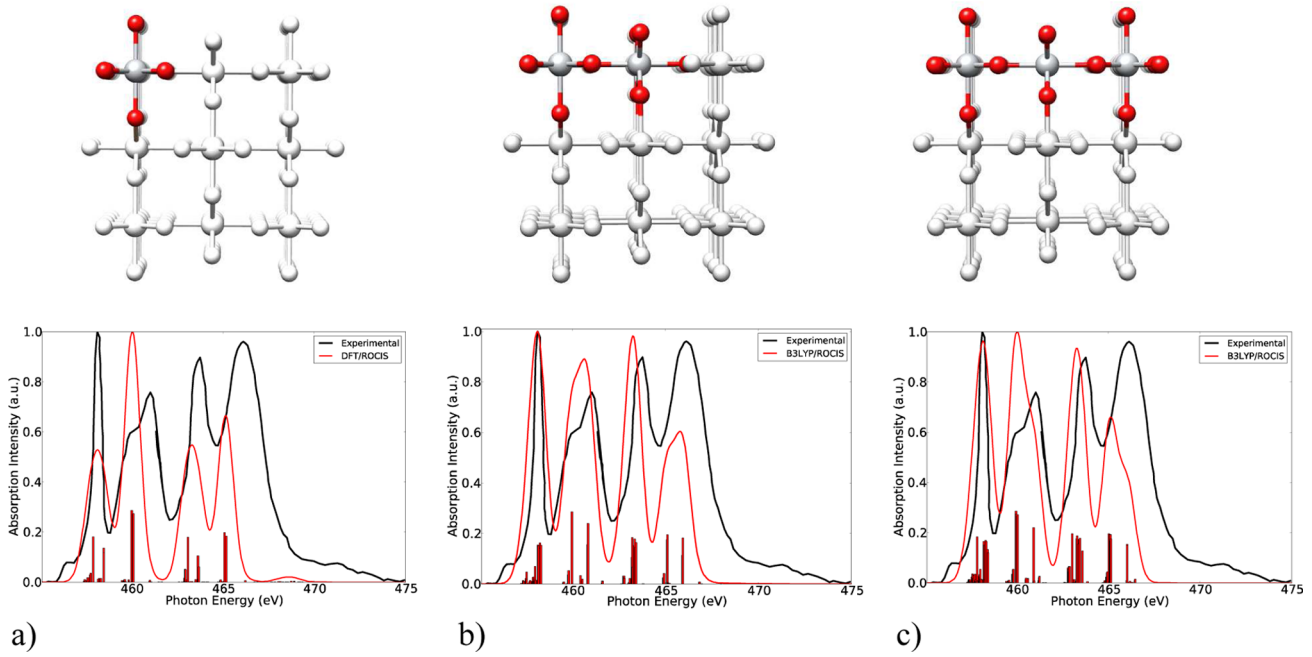

Figure 9. Experimental (black line) versus calculated (red line) B3LYP/ROCIS [def2-TZVP(-f)] Ti L-edge spectra of TiO_2 rutile: (a) monomeric, (b) dimeric, and (c) trimeric fragments along the (110) direction of the $[(Ti_{23}O_{80})^{68-} + (BR_3 + PC_3)]^0$ embedded cluster.

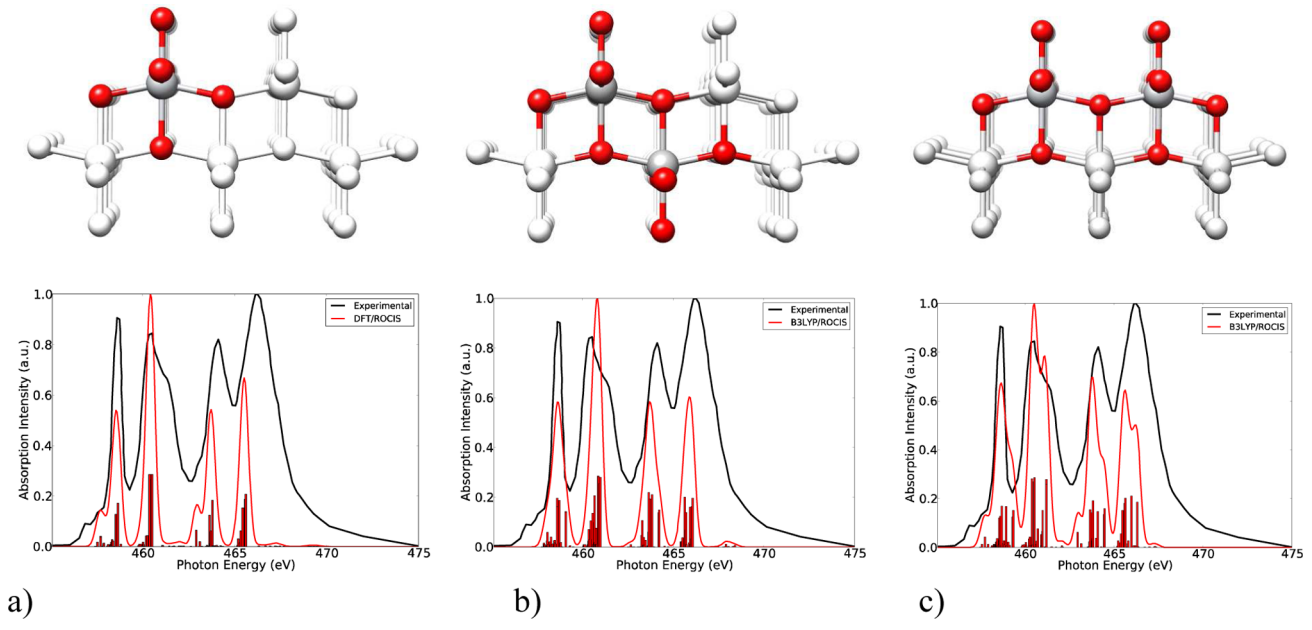

Figure 10. Experimental (black line) versus calculated (red line) B3LYP/ROCIS [def2-TZVP(-f)] Ti L-edge spectra of TiO_2 anatase: (a) monomeric and (b) dimeric fragments along (001) and (c) fragments along (100) of the $[(Ti_{15}O_{56})^{52-} + (BR_4 + PC_4)]^0$ embedded cluster.

repeated units $[Ti_2O_{10}H_8]$ are considered (Figure 7b), indicating that the Ti L-edge spectrum of bulk TiO_2 rutile and/or anatase is sensitive to the coordination environment around the titanium center.

b). Embedded Clusters. In order to explore such effects further, it is important to investigate the contributions of certain fragments within the chosen cluster to the total spectrum. This is better done via the embedding technique, which is able to describe the metal clusters in a homogeneous way, taking into account the lattice effects and avoiding unrealistic hydrogen terminations. Furthermore, several contributions arising from monomeric as well as dimeric and trimeric bridged fragments, which grow along the different crystal directions for rutile and anatase, are investigated (Figures 9 and 10). Three characteristic cases are presented in Figure 9a–c for the cases of TiO_2 rutile by employing the embedded $[(Ti_{23}O_{80})^{68-} + (BR_3 + PC_3)]^0$ cluster. As can be seen in Figure 9a, monomeric species or clusters growing along the (001) crystal direction result in a $SrTiO_3$-type spectrum, which reflect a highly symmetric octahedrally coordinated $[TiO_6]^{2-}$ titanium center.[11,19,62] On the other hand, dimeric oxygen-bridged fragments developing along the $(1\bar{1}0)$ and/or $(\bar{1}10)$ directions lower further the symmetry around the titania centers. As a result, the expected splitting and intensity ratio of

dx.doi.org/10.1021/ic500197v | Inorg. Chem. 2014, 53, 6374−6385

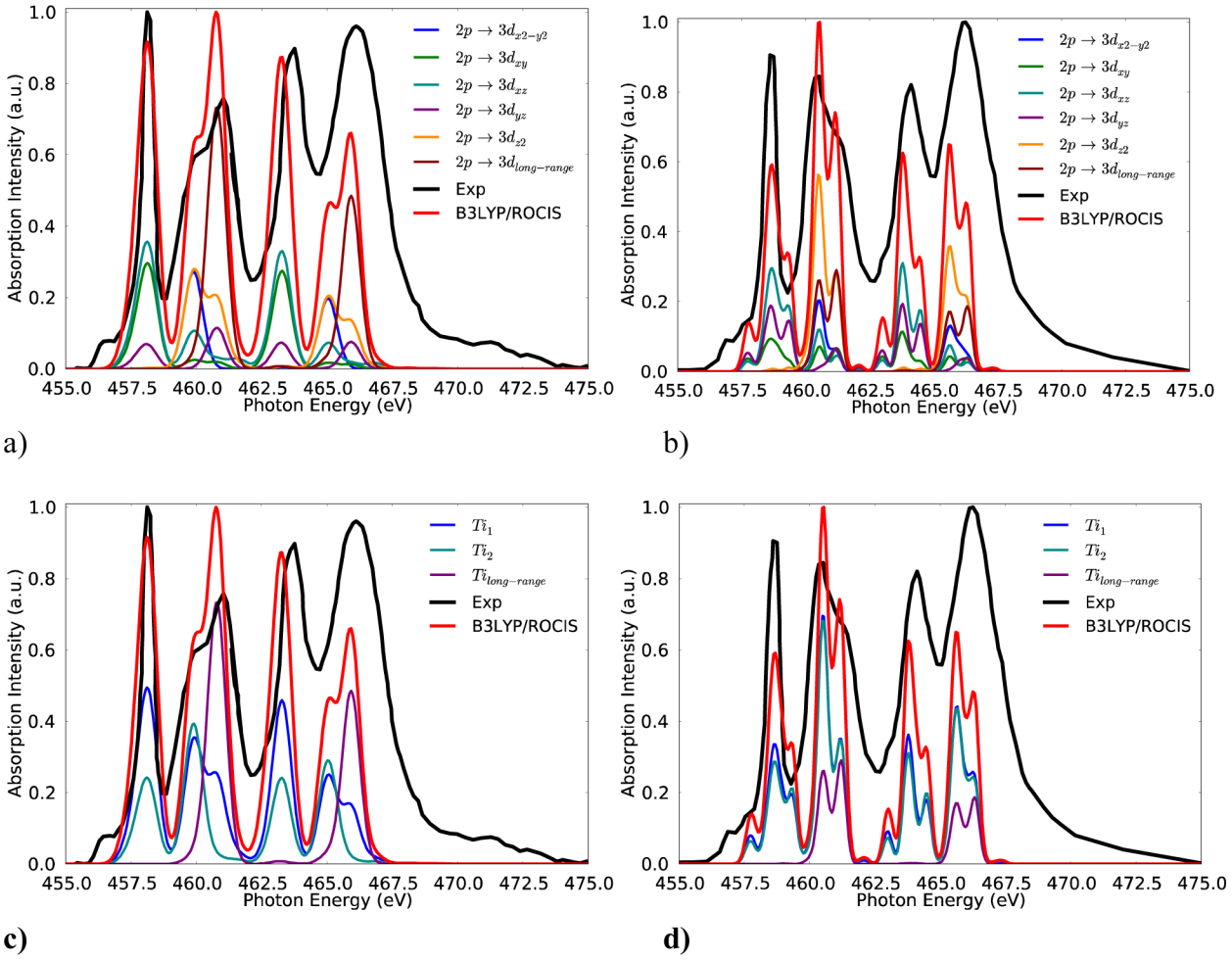

Figure 11. Calculated (red) versus experimental spectra (black) for TiO_2 rutile (left) and TiO_2 anatase (right). Blue, green, cyan, purple, orange, and dark-red lines represent deconvolution of the calculated spectrum either in terms of dominating 2p → 3d single-electron excitations (a and b) or in terms of atom contributions (c and d). Here, Ti_1 and Ti_2 refer to contributions arising from excitations involving the two titanium centers of the dimeric fragments. On the other hand, $Ti_{long\text{-}range}$ refer to contributions arising from excitations involving the rest of the titanium atoms of the studied polymetallic clusters.

the overlapping signals located at 460 and 461 eV are reproduced. Considering further trimeric clusters, the ratio of the overlapping signals is interchanged and an anatase-type signal is now observed. Similarly for TiO_2 anatase [by employing the embedded cluster $[(Ti_{15}O_{56})^{52-} + (BR_4 + PC_4)]^0$], the intensity of the overlapping signals is not reproduced, unless dimeric fragments growing along the 001 (and or 010) directions are considered. This is a clear indication that the shape of the Ti L-edge spectra and the spectral differences between rutile cannot be solely explained on the basis of the size of the employed cluster. Thus, in agreement with recent studies,[23] it seems that a balanced contribution from local and nonlocal effects dominates the intensity mechanism of these spectra, and it will be further investigated below. Furthermore, it can be concluded that qualitatively both hydrogen saturation and embedding techniques converge to identical spectra when certain fragments are considered.

Nature of Core to Valence Features. In this section, the intensity distribution of the Ca and Ti L-edge spectra of CaF_2 and TiO_2 rutile and anatase is analyzed in detail. For this purpose, DFT/ROCIS results are used throughout. In particular, we employ the central monomeric fragment of the $[(Ca_9F_{48})^{30-} + (BR_2 + PC_2)]$ embedded cluster, as well as the dimeric fragments of the $[(Ti_{23}O_{80})^{68-} + (BR_3 + PC_3)]^0$ and $[(Ti_{15}O_{56})^{52-} + (BR_4 + PC_4)]^0$ embedded clusters shown in Figures 2b, 9b, and 10c, respectively. As we have discussed recently for a series of mononuclear vanadium complexes, the metal L-edge spectra are dominated by a large number of states that reflect the local electronic structure of the metal centers.[30] It is thus desirable to characterize these states in terms of their spin multiplicities S ($S = 2S + 1$), their magnetic quantum numbers M_S, and their dominant single-electron 2p → 3d excitation character. This is possible because in most of the cases the calculated many-particle states are characterized by a small or moderately small multiconfigurational character. Moreover, the local as well as the nonlocal character (stated below as long range) of these states will be thoroughly discussed.

As can be seen in Figure S2 (Supporting Information), through tracking of the nonrelativistic character of the calculated SOC-corrected states, it becomes evident that the spectra of CaF_2, TiO_2 rutile, and TiO_2 anatase are dominated by both ground and higher multiplicity singlet and triplet states. It is noteworthy that, in all three cases, only half of the calculated intensity derives from ground singlet states, which is

dx.doi.org/10.1021/ic500197v | Inorg. Chem. 2014, 53, 6374−6385

expected because for a closed-shell d^0 complex there is an equal probability of generating a core to a valence excited singlet or triplet state under SOC mixing. In an alternative description, because the total spin is a good quantum number in each of these states, it is more appropriate to refer to the contributing final states by their M_S component rather than by their spin multiplicity prior to SOC treatment. In fact, any state of multiplicity S is mixed through QDPT, and any remaining spin degeneracy prior to SOC treatment is altered. As is seen in Figure S3 (Supporting Information), the calculated spectra of CaF_2, TiO_2 rutile, and TiO_2 anatase are dominated by the ground magnetic sublevels, respectively, containing, in addition, contributions from the corresponding relevant magnetic sublevels of the following characters: 39% $|\pm1\rangle$, 34% $|\pm1\rangle$ and 38% $|\pm1\rangle$. In a second step of analysis, the spectra can be deconvoluted in terms of the dominant 2p → 3d excitations. These excitations can be further categorized in terms of local and nonlocal contributions, as reflected in Figures 11a,b and S4 (Supporting Information). It must be emphasized that the valence MOs are distributed over the several metallic centers of the polymetallic cluster networks. As a result, the generated nonrelativistic many-particle CI states will also contain excitations into essentially delocalized valence orbitals. The transition-dipole integrals in these states might have nonzero intensity, and in the presence of a polymetallic solid system, the associated integrals might contribute essentially to the intensity mechanism. In this respect, a "local" contribution corresponds to the situation in which an acceptor orbital contains primary contributions from the same metallic center as the donor orbital, whereas a nonlocal effect (referred to here also as long-range interaction) describes the situation in which an acceptor orbital contains primary contributions from metallic centers other than the donor orbital.

For CaF_2, analysis of the individual excitations indicates cubic symmetry around the calcium center, which is consistent with a reversed O_h-symmetric ligand-field picture given in Figure 4. The lower-energy features of the L_3 region located at 347.6 and 348.2 eV are dominated by the states 55% $|0\rangle$, 45% $|\pm1\rangle$ and 52% $|0\rangle$, and 48% $|\pm1\rangle$ involving the 2p → $3d_{z^2}$ and 2p → $3d_{x^2-y^2}$ single-electron excitations. On the other hand, the main L_3 feature located at 349.1 eV is dominated by overlapping states of 66% $|0\rangle$ and 34% $|\pm1\rangle$ character involving the 2p → $3d_{xy}$, 2p → $3d_{xz}$, and 2p → $3d_{yz}$ excitations. In addition, only 6% of the dominant 2p → 3d excitations over the entire spectrum corresponds to long-range interactions. This clearly indicates that nonlocal effects are of negligible importance to describe the Ca L-edge spectrum of CaF_2. This is seen more clearly in Figure S4 (Supporting Information), in which the individual atom contributions to the spectra are visualized. Analogously for TiO_2 rutile and TiO_2 anatase, the overall excitation pattern reflects the LFT picture of titanium in a distorted O_h coordination environment (D_{2h} and C_{2v}, respectively). In both cases, the lowest-energy signals of the L_3 region located at 456−457 and 458 eV are dominated by 66% $|0\rangle$ and 34% $|\pm\rangle$ character involving the 2p → $3d_{xy}$, 2p → $3d_{xz}$, and 2p → $3d_{yz}$ excitations. Furthermore, the overlapping signals located at 460 and 461 eV are dominated by 75% $|0\rangle$ and 25% $|\pm1\rangle$ involving mainly contributions from the 2p → $3d_{z^2}$ and 2p → $3d_{x^2-y^2}$ excitations. In particular, the signal at 460 eV for both rutile and anatase is dominated mainly by the 2p → $3d_{z^2}$ and 2p → $3d_{x^2-y^2}$ excitations containing significant contributions from the 2p → $3d_{xy}$ and 2p → $3d_{xz/yz}$ excitations, respectively. On the other hand, the signal at 461 eV is subjected to the 2p → $3d_{z^2}$ excitations with some additional contribution from the 2p → $3d_{xy}$ 2p → $3d_{yz/xz}$ excitations. It should be noted that the mixing of the character of these states is (as expected) much more pronounced in anatase than in rutile because ot the lower symmetry of the local coordination environment. Nonlocal effects are also significant, and they affect the overlapping signals at 460 and 461 eV in both rutile and anatase. This is consistent with previous studies in which nonlocal effects have been claimed to govern the intensity mechanism of these signals[23] and is best seen from the atomic contributions visualized in Figures 11c,d and S4 (Supporting Information). In particular, for TiO_2 rutile, the nonlocal effects increase to about 80% of the intensity of the 461 eV signal. As a result, the intensity ratio of the overlapping signals is interchanged. In contrast, for TiO_2 anatase, the nonlocal effects contribute to the intensity of both overlapping signals by around 35%. As a result, the overlapping signals preserve the intensity ratio increases considering only local effects. It is important to observe that for the studied clusters both local and nonlocal effects are equally significant for the intensity interpretation of the overlapping signals. It is clear that local effects result in an anatase-like signal, while nonlocal effects converge to a rutile-like signal at low symmetries (e.g., in anatase). Apparently, both of them are important; however, it can be concluded that for TiO_2 rutile the shape of the overlapping signals is dominated primarily by nonlocal effects, while the opposite occurs for TiO_2 anatase.

CONCLUSIONS

In this work, we presented a systematic theoretical study on the Ca and Ti L-edge XAS spectra of CaF_2, TiO_2 rutile, and TiO_2 anatase by applying the ROCIS and DFT/ROCIS methodologies. In all cases, very good agreement between and theory and experiment was observed by employing a general theoretical protocol that involves large cluster sizes (up to 9, 23, and 15 metal for CaF_2, TiO_2 rutile, and TiO_2 anatase, respectively), as well as special charge neutralization (hydrogen saturation and embedding techniques). The calculated spectra were analyzed in terms of dominant magnetic sublevels in variable spin multiplicities and magnetic quantum numbers. These results were further mapped into a ligand-field picture, providing contributions from the leading single-electron 2p to 3d excitations. The observed spectral features were further analyzed for their origin because of local and nonlocal effects. Local effects arise from states dominated by donor−acceptor orbitals of the same atomic center. They, thus, probe the chemical environment surrounding the metal center. On the other hand, nonlocal effects involve long-range interactions between states originating from donor−acceptor orbitals located on different atomic centers. Both of these effects proved to be of paramount importance in order to successfully interpret the spectroscopies properties as well as the electronic structure of extended solid systems. In particular, the Ca L-edge spectrum of CaF_2 was found to be sensitive to only local effects, which involve a balanced description of the Ca−F bond covalency and surface/bulk interactions from the surrounding $[CaF_8]$ units. On the other hand, successful interpretation of the Ti L-edge spectra of TiO_2 rutile and anatase requires the intensity mechanism to be considered in terms of both local and nonlocal effects. In a broader perspective, the consistency of ROCIS and DFT/ROCIS methods to interpret the metal L-edge spectra of various open- and closed-shell transition-metal complexes and solids provides a strongly predictive and

dx.doi.org/10.1021/ic500197v | Inorg. Chem. 2014, 53, 6374−6385

quantitative tool with general applicability in the fields of bioinorganic chemistry and heterogeneous catalysis.

■ ASSOCIATED CONTENT

Supporting Information

Experimental versus calculated spectra. This material is available free of charge via the Internet at http://pubs.acs.org.

■ AUTHOR INFORMATION

Corresponding Author

*E-mail: frank.neese@cec.mpg.de.

Notes

The authors declare no competing financial interest.

■ ACKNOWLEDGMENTS

The authors gratefully acknowledge financial support of this work by the Max Planck Society. The reviewers of the manuscript are thanked for their constructive comments.

■ REFERENCES

(1) de Groot, F. M. F.; Kotani, A. *Core Level Spectroscopy of Solids*; CRC Press: Boca Raton, FL, 2008.
(2) Krause, M. O.; Oliver, J. H. *J. Phys. Chem. Ref. Data* **1979**, *8*, 329.
(3) de Groot, F. M. F. *J. Electron Spectrosc. Relat. Phenom.* **1994**, *67*, 529.
(4) de Groot, F. M. F. *Coord. Chem. Rev.* **2005**, *249*, 31.
(5) Thole, B. T.; van der Laan, G. *Phys. Rev. A* **1988**, *38*, 1943.
(6) Thole, B. T.; van der Laan, G. *Phys. Rev. B* **1988**, *38*, 3158.
(7) van der Laan, G.; Thole, B. T.; Sawatzky, G. A.; Verdaguer, M. *Phys. Rev. B* **1988**, *37*, 6587.
(8) De Francesco, R.; Stener, M.; Fronzoni, G. *Surf. Sci.* **2011**, *605*, 500.
(9) Fronzoni, G.; Stener, M.; Decleva, P.; Wang, F.; Ziegler, T.; van Lenthe, E.; Baerends, E. J. *Chem. Phys. Lett.* **2005**, *416*, 56.
(10) Landmann, M.; Rauls, E.; Schmidt, W. G. *J. Phys.: Condens. Matter* **2012**, *24*, 195503.
(11) Laskowski, R.; Blaha, P. *Phys. Rev. B* **2010**, *82*, 205104.
(12) Vinson, J.; Rehr, J. J. *Phys. Rev. B* **2012**, 86.
(13) Brik, M. G.; Ogasawara, K.; Ikeno, H.; Tanaka, I. *Eur. Phys. J. B* **2006**, *51*, 345.
(14) Ikeno, H.; Mizoguchi, T.; Koyama, Y.; Kumagai, Y.; Tanaka, I. *Ultramicroscopy* **2006**, *106*, 970.
(15) Ikeno, H.; Mizoguchi, T.; Tanaka, I. *Phys. Rev. B* **2011**, *83*, 155107.
(16) Ikeno, H.; Tanaka, I. *Phys. Rev. B* **2008**, *77*, 075127.
(17) Ikeno, H.; Tanaka, I.; Koyama, Y.; Mizoguchi, T.; Ogasawara, K. *Phys. Rev. B* **2005**, *72*, 075123.
(18) Kumagai, Y.; Ikeno, H.; Oba, F.; Matsunaga, K.; Tanaka, I. *Phys. Rev. B* **2008**, *77*, 155124.
(19) Ogasawara, K.; Iwata, T.; Koyama, Y.; Ishii, T.; Tanaka, I.; Adachi, H. *Phys. Rev. B* **2001**, *64*, 115413.
(20) Miedema, P. S.; Ikeno, H.; de Groot, F. M. F. d. *J. Phys.: Condens. Matter* **2011**, *23*, 145501.
(21) Bagus, P. S.; Freund, H.; Kuhlenbeck, H.; Ilton, E. S. *Chem. Phys. Lett.* **2008**, *455*, 331.
(22) Haverkort, M. W.; Zwierzycki, M.; Andersen, O. K. *Phys. Rev. B* **2012**, *85*, 165113.
(23) Krüger, P. *Phys. Rev. B* **2010**, *81*, 125121.
(24) Krueger, P.; Natoli, C. R. *Phys. Rev. B* **2004**, *70*, 245120.
(25) Natoli, C. R.; Benfatto, M.; Brouder, C.; Lopez, M. F.; Foulis, D. L. *Phys. Rev. B: Condens. Matter Mater. Phys.* **1990**, *42*, 1944.
(26) Shirley, E. L. *J. Electron Spectrosc. Relat. Phenom.* **2005**, *144*−*147*, 1187.
(27) Soininen, J. A.; Shirley, E. L. *Phys. Rev. B* **2001**, *64*, 165112.
(28) Maganas, D.; Roemelt, M.; Havecker, M.; Trunschke, A.; Knop-Gericke, A.; Schlogl, R.; Neese, F. *Phys. Chem. Chem. Phys.* **2013**, *15*, 7260.
(29) Roemelt, M.; Neese, F. *J. Phys. Chem. A* **2013**, *117*, 3069.
(30) Maganas, D.; Roemelt, M.; Weyhermuller, T.; Blume, R.; Havecker, M.; Knop-Gericke, A.; DeBeer, S.; Schlogl, R.; Neese, F. *Phys. Chem. Chem. Phys.* **2014**, *16*, 264.
(31) Roemelt, M.; Maganas, D.; DeBeer, S.; Neese, F. *J. Chem. Phys.* **2013**, *138*, 204101.
(32) Neese, F. *Wiley Interdiscip. Rev.: Comput. Mol. Sci.* **2012**, *2*, 73.
(33) Becke, A. D. *Phys. Rev. A* **1988**, *38*, 3098.
(34) Becke, A. D. *J. Chem. Phys.* **1993**, *98*, 5648.
(35) Lee, C.; Yang, W.; Parr, R. G. *Phys. Rev. B* **1988**, *37*, 785.
(36) Schafer, A.; Horn, H.; Ahlrichs, R. *J. Chem. Phys.* **1992**, *97*, 2571.
(37) Weigend, F.; Ahlrichs, R. *Phys. Chem. Chem. Phys.* **2005**, *7*, 3297.
(38) Schäfer, A.; Huber, C.; Ahlrichs, R. *J. Chem. Phys.* **1994**, *100*, 5829.
(39) Dolg, M.; Wedig, U.; Stoll, H.; Preuss, H. *J. Chem. Phys.* **1987**, *86*, 866.
(40) Bergner, A.; Dolg, M.; Küchle, W.; Stoll, H.; Preuß, H. *Mol. Phys.* **1993**, *80*, 1431.
(41) Vogt, J.; Henning, J.; Weiss, H. *Surf. Sci.* **2005**, *578*, 57.
(42) Cromer, D. T.; Herrington, K. *J. Am. Chem. Soc.* **1955**, *77*, 4708.
(43) Pipek, J.; Mezey, P. G. *J. Chem. Phys.* **1989**, *90*, 4916.
(44) DeBeer George, S.; Petrenko, T.; Neese, F. *Inorg. Chim. Acta* **2008**, *361*, 965.
(45) DeBeer George, S.; Neese, F. *Inorg. Chem.* **2010**, *49*, 1849.
(46) Lee, N.; Petrenko, T.; Bergmann, U.; Neese, F.; DeBeer, S. *J. Am. Chem. Soc.* **2010**, *132*, 9715.
(47) Beckwith, M. A.; Roemelt, M.; Collomb, M.-N. l.; DuBoc, C.; Weng, T.-C.; Bergmann, U.; Glatzel, P.; Neese, F.; DeBeer, S. *Inorg. Chem.* **2011**, *50*, 8397.
(48) Roemelt, M.; Beckwith, M. A.; Duboc, C.; Collomb, M.-N.; Neese, F.; DeBeer, S. *Inorg. Chem.* **2011**, *51*, 680.
(49) Besley, N. A.; Peach, M. J. G.; Tozer, D. J. *Phys. Chem. Chem. Phys.* **2009**, *11*, 10350.
(50) DeBeer George, S.; Petrenko, T.; Neese, F. *J. Phys. Chem. A* **2009**, *112*, 12936.
(51) Daghrir, R.; Drogui, P.; Robert, D. *Ind. Eng. Chem. Res.* **2013**, *52*, 3581.
(52) Staemmler, V., Frenking, G., Eds.; Springer: Berlin, 2005; Vol. *12*, p 219.
(53) Fronzoni, G.; Francesco, R. D.; Stener, M. *J. Chem. Phys.* **2012**, *137*, 224308.
(54) De Francesco, R.; Stener, M.; Causa, M.; Toffoli, D.; Fronzoni, G. *Phys. Chem. Chem. Phys.* **2006**, *8*, 4300.
(55) Marian, C. M.; Wahlgren, U. *Chem. Phys. Lett.* **1996**, *251*, 357.
(56) Hess, B. A.; Marian, C. M.; Wahlgren, U.; Gropen, O. *Chem. Phys. Lett.* **1996**, *251*, 365.
(57) Neese, F. *J. Chem. Phys.* **2005**, *122*, 34107.
(58) Himpsel, F. J.; Karlsson, U. O.; McLean, A. B.; Terminello, L. J.; de Groot, F. M.; Abbate, M.; Fuggle, J. C.; Yarmoff, J. A.; Thole, B. T.; Sawatzky, G. A. *Phys. Rev. B: Condens. Matter Mater. Phys.* **1991**, *43*, 6899.
(59) van der Laan, G. *Phys. Rev. B* **1990**, *41*, 12366.
(60) Walle, L. E.; Agnoli, S.; Svenum, I.-H.; Borg, A.; Artiglia, L.; Krüger, P.; Sandell, A.; Granozzi, G. *J. Chem. Phys.* **2011**, *135*, 054706.
(61) Coster, R. D.; Kronig, L. *Physica* **1935**, *2*, 13.
(62) Crocombette, J. P.; Jollet, F. *J. Phys.: Condens. Matter* **1994**, *6*, 10811.
(63) Brydson, R.; Sauer, H.; Engel, W.; Thomass, J. M.; Zeitler, E.; Kosugi, N.; Kuroda, H. *J. Phys.: Condens. Matter* **1989**, *1*, 797.
(64) de Groot, F. M. F.; Fuggle, J. C.; Thole, B. T.; Sawatzky, G. A. *Phys. Rev. B* **1990**, *41*, 928.
(65) de Groot, F. M. F.; Figueiredo, M. O.; Basto, M. J.; Abbate, M.; Petersen, H.; Fuggle, J. C. *Phys. Chem. Miner.* **1992**, *19*, 140.